nature catalysis

Article

https://doi.org/10.1038/s41929-024-01130-7

A MOF-supported Pd_1–Au_1 dimer catalyses the semihydrogenation reaction of acetylene in ethylene with a nearly barrierless activation energy

Received: 5 April 2023

Accepted: 19 February 2024

Published online: 29 March 2024

Check for updates

Jordi Ballesteros-Soberanas[1,6], Nuria Martín[2,6], Matea Bacic[1,6], Estefanía Tiburcio[2], Marta Mon[1], Juan Carlos Hernández-Garrido[3], Carlo Marini[4], Mercedes Boronat[1], Jesús Ferrando-Soria[2], Donatella Armentano[5] ✉, Emilio Pardo[2] ✉ & Antonio Leyva-Pérez[1] ✉

The removal of acetylene from ethylene streams is key in industry for manufacturing polyethylene. Here we show that a well-defined Pd_1–Au_1 dimer, anchored to the walls of a metal–organic framework (MOF), catalyses the selective semihydrogenation of acetylene to ethylene with ≥99.99% conversion (≤1 ppm of acetylene) and >90% selectivity in extremely rich ethylene streams (1% acetylene, 89% ethylene, 10% H_2, simulated industrial front-end reaction conditions). The reaction proceeds with an apparent activation energy of ~1 kcal mol^{-1}, working even at 35 °C, and with operational windows (>100 °C) and weight hourly space velocities (66,000 ml g_{cat}^{-1} h^{-1}) within industrial specifications. A combined experimental and computational mechanistic study shows the cooperativity between both atoms, and between atoms and support, to enable the barrierless semihydrogenation of acetylene.

Polyethylene is one of the most demanded chemicals worldwide, with an estimated annual production >100 million tonnes[1]. Thus, ~140 million tonnes of ethylene must be produced every year, mainly by catalytic cracking, which also produces variable amounts of acetylene (>1%) and H_2 (>20%)[2]. This ethylene stream needs to be purified before polymerization, and thus the selective semihydrogenation reaction of acetylene in ethylene flows is one of the highest volume processes in petrochemistry. Although this hydrogenation reaction is thermodynamically favoured (ΔH°_{298} = −172 kJ mol^{-1}), a catalyst is required, not only to overcome kinetic barriers but also to control the selectivity of the process, because other undesired reactions, such as ethylene hydrogenation, direct hydrogenation of acetylene to ethane and dimerization, are also thermodynamically favourable (ΔH°_{298} = −136, −308 and −173 kJ mol^{-1}, respectively). The solid catalyst currently used in industry is composed of palladium and silver species, together with other additives (sodium, calcium, etc.), and the resulting exit stream must contain <1 ppm of acetylene and <2% of ethane to be industrially acceptable[3]. Both a reaction temperature <60 °C and a weight hourly space velocity (WHSV) >50,000 ml g_{cat}^{-1} h^{-1} are required to avoid overhydrogenation reactions and undesired polymerizations (formation of green

[1]Instituto de Tecnología Química, Universidad Politècnica de València–Consejo Superior de Investigaciones Científicas, Valencia, Spain. [2]Departamento de Química Inorgánica, Instituto de Ciencia Molecular, Universidad de Valencia, Paterna, Spain. [3]Departamento de Ciencia de los Materiales e Ingeniería Metalúrgica y Química Inorgánica, Facultad de Ciencias, Universidad de Cádiz, Campus Universitario Puerto Real, Puerto Real, Spain. [4]CELLS–ALBA Synchrotron, Barcelona, Spain. [5]Dipartimento di Chimica e Tecnologie Chimiche, Università della Calabria, Rende, Cosenza, Italy. [6]These authors contributed equally: Jordi Ballesteros–Soberanas, Nuria Martín, Matea Bacic. ✉e-mail: donatella.armentano@unical.it; emilio.pardo@uv.es; anleyva@itq.upv.es

oil, coke), which would deactivate the solid catalyst. In addition, an operational temperature window of typically 35–100 °C is required to control potential runaways during the high-volume process. All these strict requirements. together with the complexity of the solid catalyst currently in use. have spurred the scientific community to look for catalysts and predictable molecular mechanisms. Thus, the surge in publications on the topic during the last ten years is not surprising (see below).

In this context, it is still difficult to find a catalyst able to accomplish the above-mentioned industrial requisites for the acetylene semihydrogenation reaction, particularly under front-end (acetylene- and H_2-rich) reaction conditions. A survey of the open literature shows a plethora of solid catalysts with different metal compositions, carriers and diverse operating conditions (feed composition, temperature, WHSV, etc.), but none of them matches, in full, the requisites outlined above. One recent review[2] and a recent publication[4] summarize the most relevant data (reactant composition, reaction temperature, acetylene conversion, selectivity and catalyst productivity) for >100 catalytic systems. We also summarize here (see below) some other relevant and very recent examples[4–27]. Recognizing the tremendous scientific information and the potential of these catalytic systems after further optimization, the provided results are, in many cases, very far from any industrial use. For instance, acetylene conversions >99% are generally provided, but the specification of ≤1 ppm of acetylene in the final stream (≥99.99% conversion) is rarely seen. Furthermore, many reports repeatedly employ a diluting inert gas or remove ethylene from the stream (just using acetylene) for a better selectivity control, which is of course not a realistic approach. Tail-end reaction conditions (using just a slight excess of H_2) are also employed to minimize ethylene hydrogenation, however, at the expense of boosting undesired polymerizations. Moreover, reaction temperatures are commonly >100 °C to increase productivity, and indeed low-temperature reactions are claimed when working below 100 °C, when the industrial process is operated at just 55 °C.

Analysis of the literature also shows that catalyst design for the acetylene semihydrogenation reaction is strongly dominated by two concepts: isolated single catalytic sites[5–7,11–13,16,20,23] and electronic catalyst modulation by alloying[8–10,18,21,22,24–27]. Both concepts follow the same mechanistic direction, which involves the preparation of catalytic metal sites at which a rapid desorption of the ethylene product occurs, without compromising the natural fast acetylene adsorption and H_2 dissociation on the metal. Indeed, the currently used solid catalyst apparently joins both concepts by diluting palladium sites on silver aggregates, with additional modifiers to regulate selectivity[3]. Different palladium alloys have been described to catalyse the reaction with enhanced activity in comparison to the non-alloyed counterparts, and, in particular, Pd_1 single atoms supported on different metal clusters and nanoparticles have shown superb catalytic activity (see below)[5–7]. It is accepted in the literature that Pd_1 can dissociate H_2 (refs. 11,12,20,23,28), and thus palladium ensembles are no longer required. As a consequence, the ultimate frontier of joining catalytic site isolation and alloying would be a palladium heterodimer, that is, Pd_1–M_1 (M = metal), where M tunes the catalytic activity of palladium. Indeed, a recent machine-learning study[29] has shown that metal dimers, such as Pd_1–Au_1, should be optimal catalysts for the acetylene semihydrogenation reaction, and a very recent experimental study employs catalytic Pd_1–Cu_1 dimers on nanodiamond graphene supports[27].

Metal–organic frameworks (MOFs) are porous crystalline materials with extremely high surface areas[30]. They also exhibit a very interesting host–guest chemistry[31]—a direct consequence of their functional empty space—that permits their use as chemical nanoreactors to produce/stabilize unprecedented metal chemical species[32]. Following this approach, our groups have recently reported the formation of well-defined palladium[33] and platinum[34] single-atom catalysts supported on MOFs, and also catalytic Pt_2 (ref. 35) and Ag_2 (ref. 36) dimers, with extremely high dispersion and metal loadings (up to 13 wt%). Thus, it seemed plausible to us to attempt the synthesis of an heterometallic Pd_1–M_1 dimer to test the catalytic semihydrogenation of acetylene. Here we show the synthesis of a well-defined Pd_1–Au_1 dimer, with >20 wt% loadings, on a MOF derived from the amino acid *S*-methyl-L-cysteine, which is stabilized through thioether linkages inside narrow (~0.6 nm) diameter pores. This solid material catalyses the semihydrogenation of acetylene under simulated front-end industrial conditions, from 35 to up to 150 °C, with ≥99.99% conversion and >90% selectivity under optimized reaction conditions, giving ethane as the only by-product. The reaction proceeds with an apparent activation energy (E_a) of ~1 kcal mol^{-1}, and is thus nearly barrierless, and experimental and computational studies support that Pd_1 is the main adsorption site during the whole mechanism, and that Au_1 and MOF sulfur atoms act as electronic modifiers for Pd_1, assisting during the key H_2 dissociation step.

Results

Synthesis and characterization of Pd_1Au_1@1

A highly robust and crystalline MOF with the formula $\{Cu_6Sr[(S,S)\text{-mecysmox}]_3(OH)_2(H_2O)\}\cdot 15H_2O$ (**1**) (mecysmox = bis[*S*-methylcysteine] oxalyl diamide)[33] was used as a chemical nanoreactor for the in situ sequential formation of the Pd_1–Au_1 dimers, which are retained and stabilized by the thioalkyl groups decorating MOF channels (Fig. 1), with the aim of producing an effective and competitive catalyst for the acetylene semihydrogenation reaction (see Supplementary Fig. 1, Supplementary Table 1 and Supplementary Discussion for more context). As a consequence, a new host–guest aggregate, with the formula $Pd_{0.5}Au_{0.5}$@$\{Sr^{II}Cu^{II}_6[(S,S)\text{-mecysmox}]_3(OH)_2(H_2O)\}\cdot 12H_2O$ (**Pd_1Au_1@1**) (Fig. 1b,e), was finally obtained. The synthetic strategy relies on a dual-step postsynthetic process consisting first of the successive insertion of Au(I) and Pd(II) salts within the MOF's channels and concomitant in situ reduction with $NaBH_4$, to form Pd_1–Au_1 dimers inside the MOF. The homogeneous distribution of sulfur-containing groups within the walls of the channels also allowed a homogeneous distribution of heterometallic Pd_1–Au_1 dimers (Supplementary Figs. 2–5). Single-crystal X-ray diffraction (SCXRD) was able to reveal the exact structure of the solid supported metal catalyst at the atomic level (Fig. 1 and Supplementary Table 2) due to the high crystallinity and robustness[13,33,37] of this kind of MOF.

Pd_1Au_1@1 is isomorphic with pristine MOF **1**, crystallizing in the chiral $P6_3$ space group, and exhibits a chiral three-dimensional strontium(II)–copper(II) network, featuring hexagonal channels of approximately 0.6 nm (Supplementary Fig. 4). The underlying net is represented by the **acs** uninodal sixfold-connected motif ($4^9.6^6$) and is built from *trans*-oxamidato-bridged dicopper(II) units of $\{Cu^{II}_2[(S,S)\text{-mecysmox}]\}$ (Fig. 1b and Supplementary Fig. 3b). The dimethyl thioether chains ensure the linkage and stabilization of the Pd_1–Au_1 dimers, which are thus uniformly distributed within the channels of the MOF (Fig. 1b–d and Supplementary Figs. 2–4).

Palladium atoms are linked by sulfur binding sites with a Pd–S bond distance of 2.41(2) Å (Fig. 1e and Supplementary Fig. 5), longer than previously observed Pd–S bond distances (2.16(2) Å)[33]. The thioether chains from the MOF are arranged in their most stable conformation in which one of the two crystallographically distinct moieties is stabilized in a bent conformation and thereby holds the palladium. In so doing, the terminal methyl groups are oriented towards the smaller interstitial voids, which are generated along the *a* axis (Fig. 1b and Supplementary Fig. 3). The other dimethyl thioether chain is stable in a more distended conformation, pointing towards the centre of the pores (Supplementary Fig. 3). These hexagonal pores allocate gold atoms situated at 3.21 Å to palladium atoms, an interatomic distance shorter than the sum of the van der Waals radii, justifying the classification as a Pd_1–Au_1 dimer, and agreeing with the tendency for palladium–gold attraction due to the net charge transfer from palladium to gold.

https://doi.org/10.1038/s41929-024-01130-7

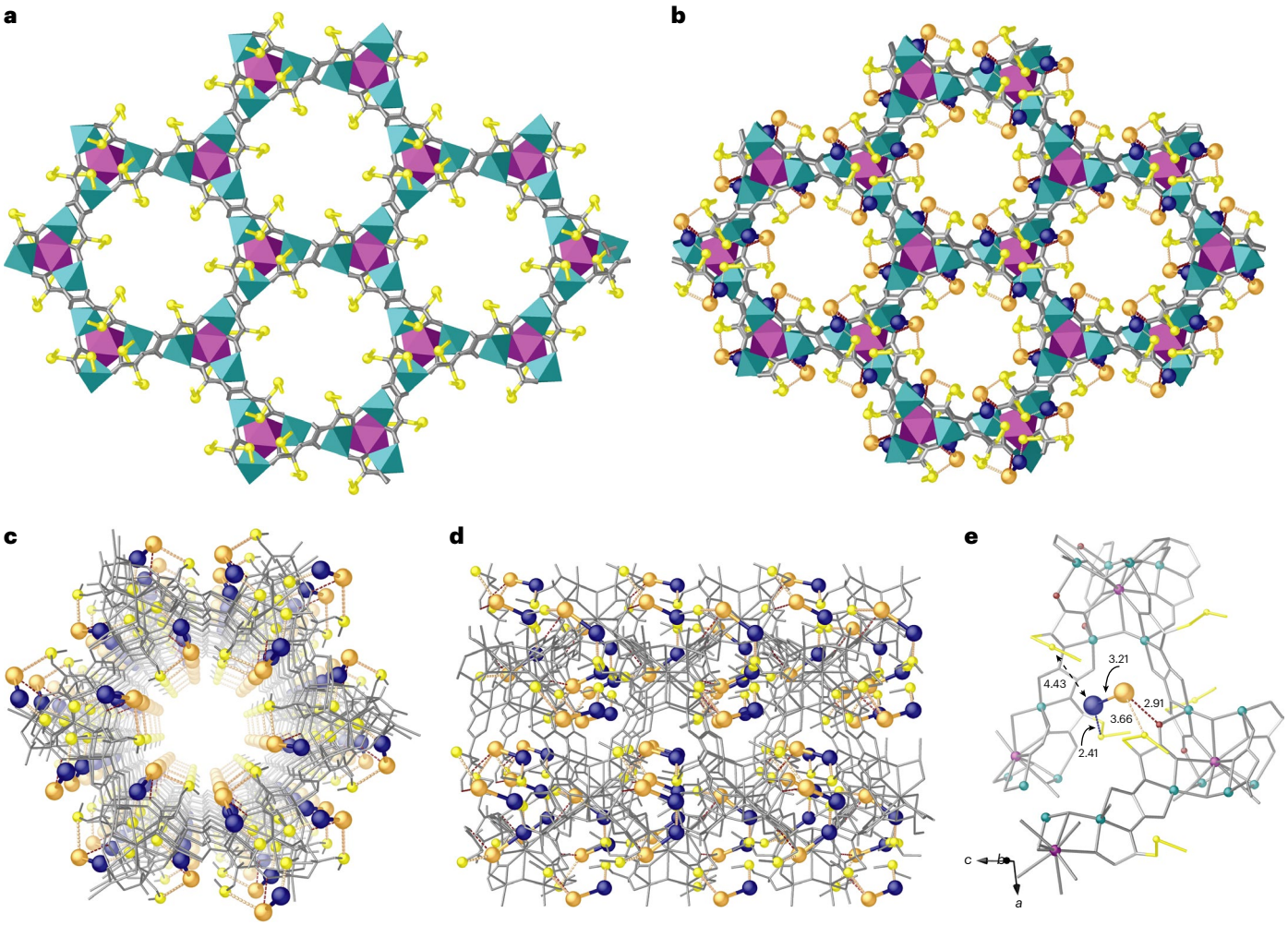

Fig. 1 | X-ray crystal structure of Pd_1Au_1@1. a,**b**, Formation of Pd_1–Au_1 dimers showing the structures of **1** (**a**) and **Pd_1Au_1@1** (**b**) determined by SCXRD. **c**,**d**, A single channel of **Pd_1Au_1@1** in the *ab* (**c**) and *bc* (**d**) plane. Copper and strontium atoms from the network are represented by cyan and purple polyedra, respectively, in **a**,**b**, whereas they are represented by grey sticks in **c**,**d**. Organic ligands are depicted as grey sticks and thioether groups as yellow sticks in all cases. Orange and blue spheres represent gold and palladium atoms, respectively, in Pd_1–Au_1 dimers. Blue, orange and red dotted lines represent the Pd···S, Au···S and Au···O interactions, respectively. **e**, Details of X-ray crystal structure showing the main host–guest interactions and related structural parameters of Pd_1–Au_1 dimers.

The gold atoms are stabilized by interactions involving oxygen atoms from the oxamate moieties, belonging to the MOF core, and delimiting the walls of the MOF at a distance of 2.91 Å. It is worth emphasizing a further Au···S distance of 3.66 Å that, although longer than the Au–S bond length, can be considered a very effective stabilizing interaction (Fig. 1e and Supplementary Fig. 5) as supported by extended X-ray absorption fine structure (EXAFS) measurements (see below). The gold atoms are stabilized by interactions involving oxygen atoms from the oxamate moieties, belonging to the MOF core and delimiting the walls of the MOF and weak sulfur binding at distances of 2.91 and 3.66 Å, respectively (Fig. 1e and Supplementary Fig. 5). No examples of a crystallographically precise Pd_1–Au_1 dimer appear to have been reported previously. Nevertheless, both the Pd···S and Au···O distances are comparable to those previously reported for palladium and gold nanoclusters[33,38]. Interpretation of the SCXRD offers a description of the palladium–gold environment with palladium atoms tetra-coordinated by Pd–S, Pd–Au and expected Pd–O_{waters} (not detected by ΔF maps as predictable for solvent molecules in porous crystals, but confirmed by EXAFS experiments) in a highly distorted environment, and with gold only linked to Pd and $O_{oxamate}$, with a coordination number of 2, in a would-be linear geometry, substantially distorted, mainly due to the effectiveness of the weak Au···S interactions described above. The geometric constraints imposed by the MOF topology and the intrinsic flexibility of the methylcysteine moieties, all possible conformations of which have been averaged in one unit cell by crystallography, contribute to promote distortion from linearity.

Density functional theory (DFT) calculations (see below) support the SCXRD data. The experimental crystal structure of **Pd_1Au_1@1** (Fig. 1e) shows that the palladium atom is linked directly to one sulfur atom from the thioether chain at 2.4 Å and resides at a longer distance, of 4.4 Å, from a second sulfur atom, and that the gold atom achieved stability at a slightly longer Au···O distance of 2.9 Å and a considerably longer Au···S separation of 3.66 Å. In contrast, the theoretical calculations indicate that the most stable system is where the palladium atom is directly linked to two sulfur atoms at similar distances of ~2.3 Å, and one thioether group at a longer Au–S distance (3.6 Å) stabilizes the gold atom. The apparent deviation between experimental (SCXRD) and theoretical (DFT calculations) results provides, however, the most realistic answer to the proposed structure of **Pd_1Au_1@1**. The intrinsic and extraordinary flexibility of the thioether chains confined in pores, detected by thermal and dynamic disorder[34], and expected in porous crystals, acts synergistically to enable the approach of the second

https://doi.org/10.1038/s41929-024-01130-7

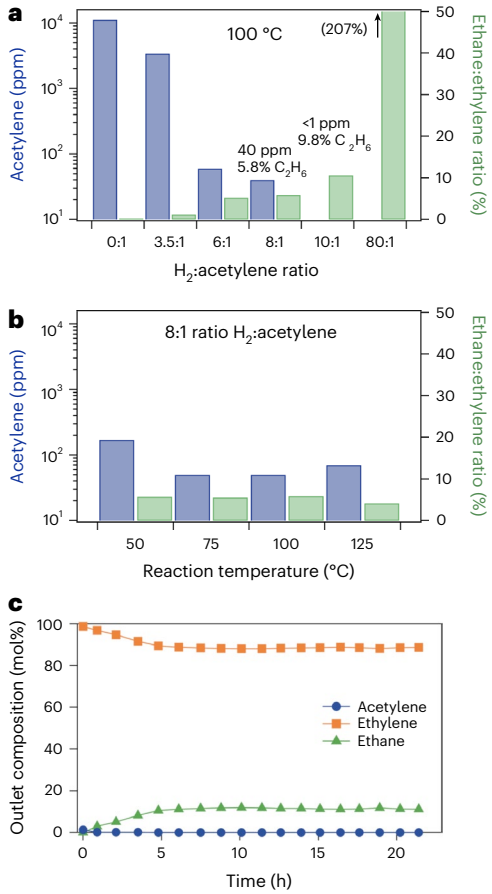

Fig. 2 | Catalytic experiments for the semihydrogenation reaction. a,**b**, Effect of H_2:acetylene stoichiometry (**a**) and temperature (**b**) on the selective acetylene hydrogenation with **Pd_1Au_1@1**. **c**, Stability over time for **Pd_1Au_1@1** under optimal reaction conditions: 10:1 H_2:acetylene ratio, 33 ml min^{-1} of 1% acetylene in ethylene, 24 h reaction time and 100 °C reaction temperature.

sulfur atom towards the palladium atom. As far as gold is concerned, it is plausible to consider a similar mechanism in which the flexibility of the methylcysteine moieties ensures the gold atoms approach the sulfur atoms, moving from a distance of 3.66 to 2.4 Å. This movement is supported by a simultaneous break of the Au···$O_{oxamate}$ interaction, which serves to first stabilize the loaded gold ions, which are then reduced to Au^0 and finally stabilized by highly dynamic thioether chains (Supplementary Fig. 5).

EXAFS measurements confirm the bonding of the metal atoms to the sulfur thioether chains (Supplementary Fig. 6). The palladium k^2 EXAFS signals (Supplementary Fig. 6a) and the corresponding relative Fourier transform (Supplementary Fig. 6b) of the PdAu–MOF, before and after a partial reduction process (involving just two $NaBH_4$ additions), show the formation of a new bond compatible with Pd–S and Pd–O, easily determined by comparison with Pd and PdO references. The formation of the new bonds is more visible in the lower k range and results in a slight change of the main peak in the Fourier transform, which is also seen in the crystallographic model for the first-shell fit of palladium (Supplementary Fig. 7). The numeric results of the fit (Supplementary Table 3) show that the typical tetra-coordination found for monometallic palladium complexes is also found in **Pd_1Au_1@1**, somewhat distorted, with sulfur (and perhaps oxygen) as the first-shell coordinated atoms. The gold EXAFS measurements were not so clear regarding the formation of Au–S bonds because the latter are less significant in **Pd_1Au_1@1** and tiny amounts of unavoidably formed gold nanoparticles masked the results (Supplementary Fig. 8). However, it can be seen that **Pd_1Au_1@1** contains significant amounts of signals compatible with Au–S bonds, in contrast to gold foil.

To unveil the oxidation states of palladium and gold in the MOF, X-ray absorption near-edge structure (XANES), X-ray photoelectron spectroscopy (XPS), diffuse reflectance infrared Fourier transform spectroscopy with CO probe (DRIFTS) and ^{13}C solid-state magic-angle spinning nuclear magnetic resonance with ^{13}CO probe (^{13}C ss-MAS-NMR) analyses were carried out.

The palladium XANES analysis of **Pd_1Au_1@1** after a partial reduction process (involving just two $NaBH_4$ additions; Supplementary Figs. 9 and 10 and Supplementary Table 4) shows the formation of an oxidized monometallic $Pd^{\delta+}$ site. The corresponding gold XANES analysis is not included here because the formation of some gold nanoparticles masks the results. The XPS spectra of **Pd_1Au_1@1** before and after complete reduction with $NaBH_4$ (Supplementary Fig. 11a,b, respectively) show that the Pd 3*d* line before reduction is a doublet with binding energies for the Pd $3d_{5/2}$ and Pd $3d_{3/2}$ of 337.5 and 342.8 eV, respectively, which are typical of Pd^{2+} cations and similar to other reported values[33]. On the other hand, the deconvolution of the Au 4*f* region shows three doublets for Au $4f_{7/2}$ and Au $4f_{5/2}$ transitions at 86.4 and 90.5 eV (first doublet), 85.3 and 89.5 eV (second), and 84.1 and 87.7 eV (third), which are attributed to Au^{3+}, Au^{+} and metallic Au^0, respectively[39], and suggests that Au^{3+} cations are already partially reduced before treating the MOF with $NaBH_4$. After reduction, the situation drastically changes for palladium and the observed doublet at 335.5 eV (Pd $3d_{5/2}$) and 340.8 eV (Pd $3d_{3/2}$) can be attributed to slightly positive $Pd^{\delta+}$ species[37,40]. Similarly, the Au 4*f* region shows a doublet at 83.5 eV (Au $4f_{7/2}$) and 87.1 eV (Au $4f_{5/2}$) that is indicative of fully reduced gold[39]. These binding energies are in full agreement with those observed for other reported AuPd bimetallic alloys[41]. Moreover, binding energies assigned to Au $4f_{7/2}$ and Au $4f_{5/2}$ in the Pd_1–Au_1 dimer (83.5 and 87.1 eV, respectively) are slightly downshifted compared with those observed, for the same regions, before reduction (84.1 and 87.7 eV, respectively). This fact suggests that gold atoms gain electronic density from palladium atoms in the dimer formation process[42]. The Au 4*f* and Pd 3*d* binding energies, and the binding energies from the O 1*s* and C 1*s* regions, are collected in Supplementary Table 5.

The DRIFTS with CO probe spectrum of **Pd_1Au_1@1** (Supplementary Fig. 12, top) shows two main signals at 1,975 and 1,872 cm^{-1}, which can be assigned to significantly reduced $Pd^{\delta+}$ and Au^0 species, respectively[37,43]. A small signal at 2,110 cm^{-1} can also be observed, which can be assigned to a small fraction of single Pd_1 atoms remaining in the material, by comparison with **Pd_1@1** (Supplementary Fig. 12, bottom). A ^{13}C ss-MAS-NMR analysis of **Pd_1@1**, unreduced AuPd–MOF and **Pd_1Au_1@1** was carried out under an atmosphere of ^{13}CO, for 8 h at room temperature. This technique makes it possible to qualitatively distinguish between partially reduced cationic sites (Lewis acid) and reduced metal sites because the intensity of CO coordinated to the former is 1-fold higher[42]. Furthermore, in the particular case of palladium and gold metals, we deliberately left a small amount of air during the measurement to obtain $^{13}CO_2$ if gold metal sites were present. The results (Supplementary Fig. 13) show that both **Pd_1@1** and the unreduced AuPd–MOF contain significant amounts of cationic sites (signals between 150 and 180 ppm) and barely generate $^{13}CO_2$ (signal at 122 ppm) but, in contrast, **Pd_1Au_1@1** contains nearly the half amount of cationic sites and forms significant amounts of $^{13}CO_2$. In other words, half of the metal content has been completely reduced to metallic valence in **Pd_1Au_1@1**, probably gold, while the other half retains some cationic charge. These results, together, match well with the proposed structure of **Pd_1Au_1@1**.

In addition to the structural characterization, the chemical nature of **Pd_1Au_1@1** was also established by various characterization techniques. Elemental analyses (C, H, S, N) and inductively coupled plasma mass spectrometry (Supplementary Table 6) confirmed the proposed chemical composition. The experimental powder X-ray

https://doi.org/10.1038/s41929-024-01130-7

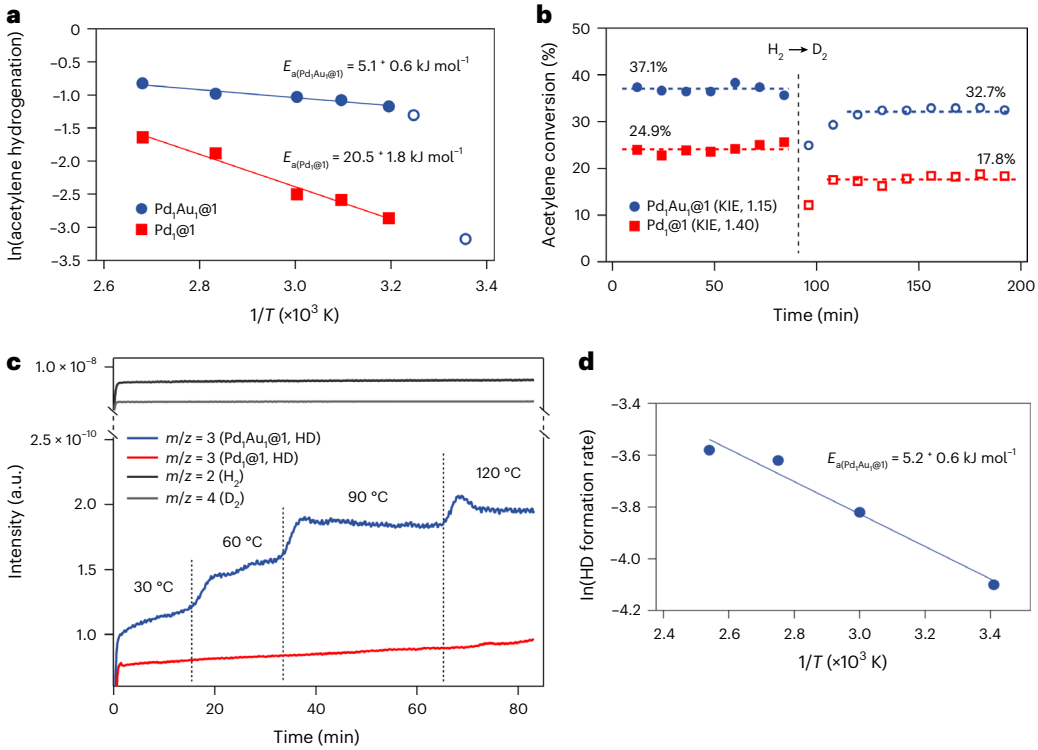

Fig. 3 | Experimental mechanistic evidence for Pd_1Au_1@1 and Pd_1@1. a, Apparent activation energy (E_a) of the overall acetylene hydrogenation reaction. **b**, Measured KIE (H_2/D_2) on the acetylene hydrogenation reaction. Filled symbols, H_2; empty symbols, D_2. **c**, Hydrogen-splitting activation energy obtained from the HD formation rates. **d**, Activation energy of the hydrogen-cleavage process.

diffraction pattern of **Pd_1Au_1@1** (Supplementary Fig. 14) matches the theoretical one, confirming both the purity and homogeneity of the bulk sample. Thermogravimetric analysis confirms the solvent content of **Pd_1Au_1@1** (Supplementary Fig. 15) and makes it possible to establish the proposed chemical formula. The total potential accessible voids in **Pd_1Au_1@1** amount to 1,274.0 Å^3, accounting for 35.6% of the unit cell volume (3,580.9 Å^3). The virtual diameter of the channels decreases from ~0.9 nm in the pristine MOF **1** to 0.56 nm in **Pd_1Au_1@1** (Supplementary Fig. 3), due to the presence of the Pd_1–Au_1 dimers within the channels, and N_2 adsorption isotherms at 77 K confirm the permanent porosity of **Pd_1Au_1@1** (Supplementary Fig. 16, top). It is worthy to notice here that this small pore size is convenient to perform the semihydrogenation of acetylene without competing coupling by-reactions, since a 0.56 nm pore size allows the entrance and diffusion of C_2 molecules but hampers the formation and diffusion of bigger molecules (Catalytic results). Competitive adsorption experiments of acetylene and ethylene at 25 °C show that just 1% of acetylene in pure ethylene produces a significant decrease in the adsorption of ethylene (Supplementary Fig. 16, middle), which suggests a stronger affinity of the MOF sites for acetylene. The Fourier transform infrared spectrum of the treated **Pd_1Au_1@1** sample shows the signals associated with acetylene adsorption (Supplementary Fig. 16, bottom).

High-angle annular dark-field scanning transmission electron microscopy was employed to analyse the **Pd_1Au_1@1** material (Supplementary Fig. 17). The results show that both palladium and gold are homogeneously distributed across the MOF according to energy-dispersive X-ray measurements, together with the other elements of the MOF (that is, sulfur and strontium). The observed weight fractions for palladium and gold are in accordance with the calculated molecular formula for **Pd_1Au_1@1** (Supplementary Fig. 18).

Catalytic results

Pd_1Au_1@1 (30 mg) was mixed with SiO_2 powder (300 mg) and loaded into a fixed-bed tubular reactor; different combinations of flow rates/H_2:hydrocarbon mixtures (C_2) and temperatures were screened to find the optimal operational conditions for the acetylene semihydrogenation reaction (Fig. 2a,b; see Supplementary Table 7 for numerical values). The reaction temperature does not have a significant impact on acetylene conversion, at least from 35 to 150 °C, which suggests a very low activation energy for the reaction on the **Pd_1Au_1@1** catalyst (Fig. 3). Dimerization peaks were not observed up to 150 °C, indicative of a lack of polymerization. Elemental analysis and extractions of the used catalyst with organic solvents (Methods) confirm the lack of formation of C_4 products, green oils or coke. Changes in the flow rate revealed that the optimal stoichiometry for H_2:acetylene was 10:1, which corresponds to typical front-end acetylene hydrogenation conditions[4]. The achieved throughput under these conditions, in terms of WHSV, was 66,000 ml g_{cat}^{-1} h^{-1}, and the acetylene left was ≤1 ppm, the detection limit of the gas chromatograph used, which corresponds to a ≥99.99% yield, with typically >90% selectivity. To assess the concentration (parts per 10^9 (ppb)) of acetylene remaining, a ten-times bigger loop was installed in the gas chromatograph; however, we were not able to assess accurately the amount of acetylene beyond values of 500–1,000 ppb, due to free induction decay signal saturation and peak overlapping. In any case, the conversion, selectivity and productivity values obtained for the **Pd_1Au_1@1** catalyst fall within industrial specifications. The stability over time of **Pd_1Au_1@1** shows a constant ≥99.99% conversion of acetylene and ~90% selectivity after a period of stabilization (Fig. 2c).

The palladium and gold metal content in **Pd_1Au_1@1** is 2.9 and 5.2 wt%, respectively (Supplementary Table 8). This very high metal content in the solid provides an evident advantage for the throughput of the in-flow reaction in terms of productivity per mass of catalyst. For the sake of comparison, MOFs containing only one type of metal atoms,

here called **Pd_1@1** (ref. 33) and **Au@1**, were also prepared and tested as catalysts (Supplementary Table 7), and since the noble metal content remains similar for these MOFs (Supplementary Table 8), the experiments can be considered comparable. The acetylene hydrogenation reaction was then performed with 36 mg of **Pd_1@1** and/or 41 mg of **Au@1** to maintain the amount of palladium and gold constant, respectively. **Pd_1@1** did not catalyse the acetylene hydrogenation at high flow rates (33 ml min^{-1}), as **Pd_1Au_1@1** does, and requires a residence time and a H_2:acetylene stoichiometry 3-fold higher (Supplementary Table 9). Under these optimized reaction conditions, **Pd_1@1** achieved a 99.6% acetylene conversion (with 40 ppm remaining) and a WHSV of 20,282 ml g_{cat}^{-1} h^{-1} (gas hourly space velocity, 5,143 h^{-1}; Supplementary Fig. 19), which are values very different to the catalytic activity of **Pd_1Au_1@1**. **Au@1** did not show any catalytic activity under all the reaction conditions tested (Supplementary Table 9) and did not change the catalytic activity of **Pd_1@1** when physically mixed with it. The stability/recyclability of **Pd_1Au_1@1** was confirmed by XPS and powder X-ray diffraction: performing these analyses after the catalytic experiments showed no significant difference with analyses performed before catalysis (Supplementary Figs. 20 and 21).

We investigated how the catalytic behaviour of the microporous **Pd_1Au_1@1** material varied with pore size. Because the preparation of a similar MOF with different-sized channels is not straightforward (the particular amino-acid-based building blocks used drive the formation of this particular MOF and not others), we prepared and tested structurally related microporous zeolites with a similar chemical composition but slightly different pore sizes. Specifically, we prepared different Pd–Au–MS materials (MS, molecular sieves) with pore sizes of 3, 5 and 7 Å. The 3 and 5 Å pore size materials correspond to typical drying agents, which contain Ca^{2+} and Na^+ as countercations, and the 7 Å pore size corresponds to zeolite NaY. H^+-zeolites were avoided to circumvent any possible Brønsted-acid-catalysed process. The palladium and gold metals were introduced by the wet impregnation method (Methods), in this metal order, and the structural integrity of the zeolite framework was confirmed by X-ray diffraction (Supplementary Fig. 22). It should be mentioned here that the metal content in the zeolites can be adjusted (from 1 to 16 wt%) to avoid metal agglomeration, and that this metal amount can be significantly lower than in **Pd_1Au_1@1** (7.1 wt% palladium). Nevertheless, the total metal amount in reaction was equalized to that in the MOF by just adding more zeolite.

The palladium- and gold-containing zeolites showed a different catalytic activity depending on the pore size. Reaction conditions were tuned to have a 90% conversion of acetylene for the **Pd_1Au_1@1** catalyst to better compare the catalytic activity of the different materials. The Pd–Au–MS 5 Å and NaY (7 Å) materials achieved complete acetylene conversion, while Pd–Au–MS 3 Å showed a conversion of 85% (Supplementary Fig. 23). The dimensions of the smaller MS support material cause limitations in achieving a complete acetylene conversion because channels that are too small in diameter can hinder the diffusion and transport of reactants and products within the catalyst structure. Consequently, acetylene molecules are less accessible to the catalytic active sites, resulting in incomplete conversions.

The ethane/ethylene ratio also increased as the pore size increased from 3 to 5 Å, with the ratio stabilizing at 7 Å pore size. Green oils were not found under any conditions. The **Pd_1Au_1@1** material (5.6 Å channel) shows an intermediate catalytic behaviour, similar to the MS 5 Å zeolite. It should be noted here that a direct catalytic comparison of the zeolites and the MOF by just considering the pore size is not entirely valid because zeolites have interconnected three-dimensional channels with cavities. It should also be noted here that the catalytic activity of **Pd_1Au_1@1** is much higher than that of any zeolite when the reaction conditions were pushed to achieve maximum production rates, even after optimizing the reaction conditions, metal content, order of incorporation (gold before palladium) or H_2 feed ratio in the zeolite (the study was done for the MS 5 Å material; Supplementary Figs. 24 and 25). These results support the hypothesis that the small pore size of the MOF combined with the formation of a high-density-number of **Pd_1Au_1** catalytic species is behind its extremely high catalytic activity.

Mechanistic studies

Kinetic and isotopic experiments were carried out. Figure 3 shows that the measured activation energy for acetylene hydrogenation with **Pd_1Au_1@1** as a catalyst is outstandingly low, 5.1 ± 0.6 kJ mol^{-1}. The lowest value we could find in the literature for any catalyst in this reaction is 17 kJ mol^{-1} (ref. 8) for a Pd_2Sn alloy material. The activation energy of silver-alloyed palladium single atoms, which is more similar to the industrial catalyst, is 40.1 kJ mol^{-1} (ref. 12). For the sake of comparison, silver-, gold- and copper-alloyed palladium single atoms have been found to have activation energies ranging from 37.3 to 38.2 kJ mol^{-1} (ref. 5). It has been reported that thioether additives increase the selectivity for acetylene[44], and hence the coordinative environment of the Pd_iAu_1 alloy must play a role.

Kinetic isotope effects (KIEs) were also measured (Fig. 3b). The results show that changing from H_2 to D_2 does not produce any significant change in the reaction rate. A very mild primary KIE (k_H/k_D = 1.15) was recorded when **Pd_1Au_1@1** was used as a catalyst, which could imply that the H–H splitting process is not the limiting step, although this cannot be asserted with certainty due to the low apparent activation energy observed. The fact that H_2 dissociation occurs easily and **Au@1** does not catalyse the reaction points to palladium as the active metal atom during the reaction because gold often requires agglomeration[45] or strong ligands[46] to dissociate H_2. When **Pd_1@1** was used, a mild primary KIE (k_H/k_D = 1.40) was measured, which indicates that the presence of gold facilitates H_2 dissociation, which is in good agreement with the observed larger activation energy (Fig. 3a).

H_2–D_2 exchange experiments were performed to accurately study the limiting nature of the H_2 dissociation process (Fig. 3c). The isotope exchange experiments revealed that the activation energy for the hydrogen-splitting process is 5.2 ± 0.6 kJ mol^{-1} for **Pd_1Au_1@1** (Fig. 3d), equal within error to the global apparent activation energy, and therefore indicating experimentally that the H_2 dissociation step limits the hydrogenation reaction: a quasi–spontaneous process. Despite using three times more sample than for **Pd_1Au_1@1** during the H_2–D_2 exchange measurement, H_2 dissociation information was not obtained with **Pd_1@1** due to the very low HD formation, which we correlate to the relatively higher H_2 flows required for acetylene hydrogenation over the **Pd_1@1** catalyst (Supplementary Table 9).

Theoretical calculations

Periodic DFT calculations of the Pd_1–Au_1 dimer within the MOF, in six different configurations, support the crystallographic characterization of **Pd_1Au_1@1** and made it possible to select a realistic model of the active site for use in the mechanistic study (Supplementary Fig. 26 and Supplementary Table 10). Pd_1–Au_1 dimers remain stable in most of the locations considered, with optimized Pd–Au bond lengths of ~2.6 Å, and with optimized Pd–S and Au–S distances of ~2.3 Å. The palladium atoms are always slightly positively charged whereas the gold atoms remain almost neutral. The most stable system obtained, labelled F, shows that the palladium atom is directly interacting with two sulfur atoms, and the gold atom is stabilized by one sulfur atom.

Once the catalytic metal site had been optimized, the mechanism of the semihydrogenation reaction of acetylene was studied with a representative fragment of the system F. The first step considered was the dissociation of molecular H_2, which takes place on the palladium atom. The most favourable binding site for H_2 is opposite to the gold atom, forming structure 1-A (Supplementary Fig. 27). However, the calculated activation energy for the H–H bond breaking in this configuration is extremely high, 208 kJ mol^{-1}, which contradicts the experimental results. Alternatively, H_2 can also bind palladium by displacing one of

https://doi.org/10.1038/s41929-024-01130-7

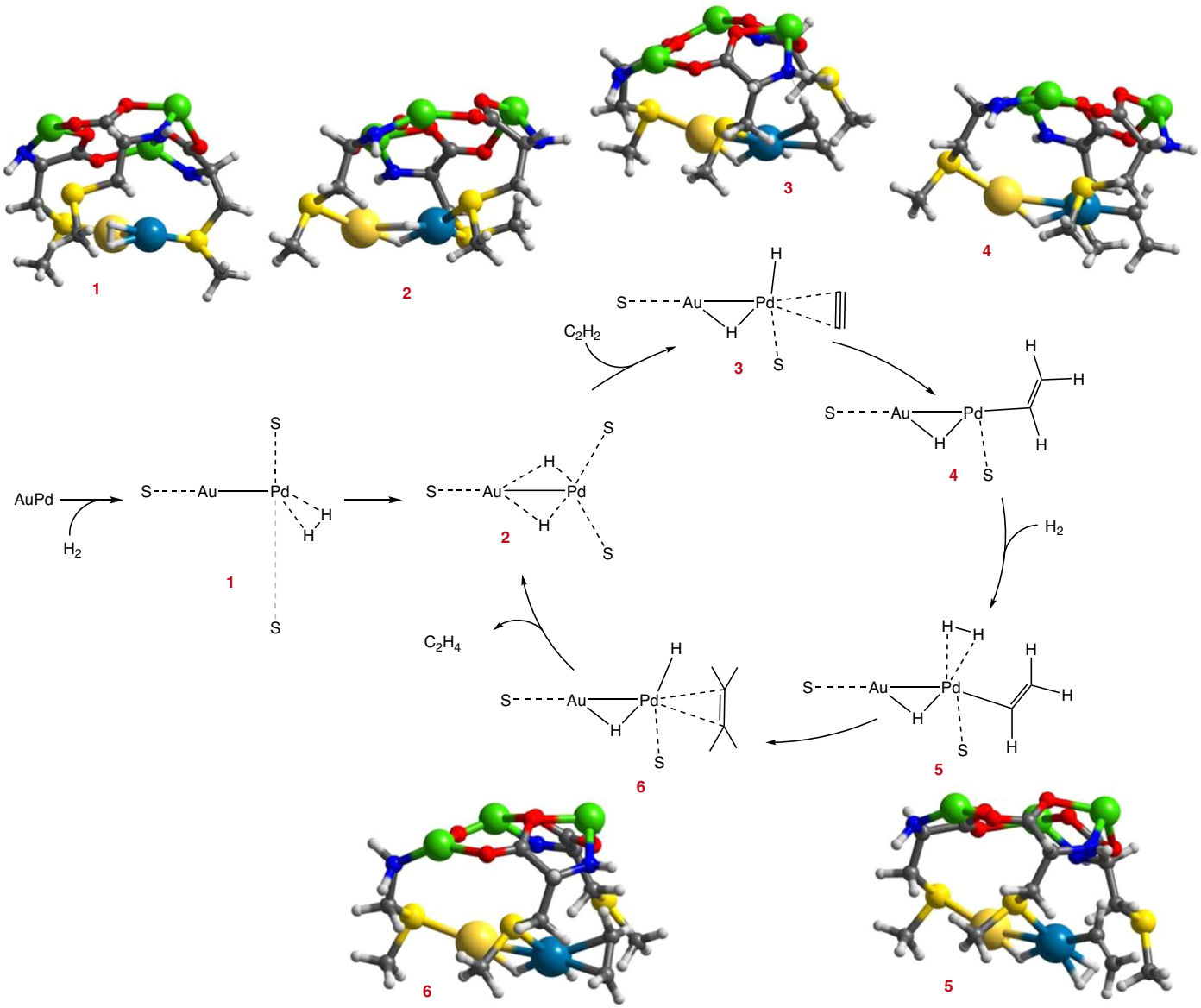

Fig. 4 | Theoretical calculations. The most plausible computed intermediates and proposed mechanism for acetylene hydrogenation with Pd_1Au_1@**1** catalyst. Gold, palladium, copper, sulfur, oxygen, nitrogen, carbon and hydrogen atoms are depicted as gold, cyan, green, yellow, red, blue, grey and white spheres, respectively.

the thioether groups to form structure 1-B. Although the adsorption complex is less stable, the activation energy necessary to dissociate H_2 following this pathway is significantly lower, 42 kJ mol^{-1} (see energy profile in Supplementary Fig. 28a), and this route can be favoured in the presence of additional H_2 molecules (pathway C in Supplementary Figs. 27 and 28).

In all cases, the product of the first elementary step is a structure, named 2, with one of the hydrogen atoms bridged between palladium and gold, and the other one either monocoordinated to palladium as in structures 2-A and 2-C, or bridged between palladium and gold as in structure 2-B (Supplementary Fig. 27). The gold atom acts as a modifier of the palladium atom, to increase the catalytic activity and selectivity[47,48], and also assists during the H–H dissociation event.

The adsorption of acetylene on structure 2-A requires the detachment of one of the thioether groups from palladium (Supplementary Fig. 29) and the transfer of the hydrogen bonded to palladium to one of the carbon atoms through transition state TS34-A, to produce intermediate 4-A, with an activation energy of 34 kJ mol^{-1}. The pathway requires the participation of a second H_2 molecule (structure 5-A in Supplementary Fig. 29), which dissociates on palladium through TS5-6, forming adsorbed ethylene together with a hydrogen atom on palladium (structure 6-A). The activation energy obtained for this step, 100 kJ mol^{-1}, is again too high compared with the experimental data. In contrast, a similar pathway starting from structure 2-B is energetically favoured, with no reaction intermediates that are too stable, and with activation energies of only 17 and 29 kJ mol^{-1} for the two elementary steps considered (see optimized geometries in Supplementary Fig. 30 and the energy profile in Supplementary Fig. 28b, orange line). The reason is that the initial detachment of one of the thioether groups from palladium facilitates the adsorption of H_2 and acetylene along the pathway. Interestingly, desorption of ethylene from structure 6-B regenerates the active intermediate 2-B with two adsorbed hydrogen atoms, and hence the initial and energetically demanding dissociation of H_2 on palladium is no longer necessary in the most plausible catalytic cycle (Fig. 4).

The competitive hydrogenation of ethylene to produce ethane was also computationally investigated. Starting from structure 6-B, the first hydrogen transfer to produce intermediate 7-B involves a low activation

energy of only 11 kJ mol^{-1} (Supplementary Figs. 31 and 32). However, the intermediate species obtained is not too stable, the necessary coadsorption of a second H_2 molecule is endothermic, and the additional activation energy necessary to dissociate H_2 and simultaneously generate ethane is 38 kJ mol^{-1}. Comparison of the energy profiles for the acetylene (orange) and ethylene (purple) hydrogenation reactions on the same active site (Supplementary Fig. 28c) shows the energetic difference between the two reactions, with ethane formation being clearly disfavoured.

It could be argued here that the cluster model used in these computational simulations cannot accurately simulate the periodic structure of the MOF, with the main drawback being the neglect of dispersion interactions. Nevertheless, the cluster approach has been widely used to model catalytic processes in MOFs where the active sites are isolated and well defined due to its lower computational cost. Therefore, we also performed the calculations by using a cluster that models accurately the main features of the active site to compare the different reaction mechanisms at a reasonable computational cost. The results confirm the accuracy of the cluster model used after recalculating the dissociation of H_2 with a periodic model of the MOF and the Vienna Ab initio Simulation Package code because both approaches lead to the same two possible pathways A and B, which differ in the mode of H_2 binding to the PdAu dimer (Supplementary Fig. 33). In pathway A, H_2 binds to the palladium atom on the opposite side of gold, forming a more stable complex 1-A that requires a higher activation energy for dissociation of the H–H bond (blue lines in Supplementary Fig. 33), whereas in pathway B, the binding of H_2 to palladium displaces one of the thioether groups resulting in a less stable system 1-B that clearly facilitates the H–H dissociation (orange lines in Supplementary Fig. 33). Comparison of periodic (full lines) with cluster (dashed lines) energy profiles shows that all intermediates and transition states are better stabilized in the more realistic periodic model, but since this effect is quite constant, the relative energies do not differ significantly. The two computational approaches lead to the conclusion that H_2 dissociation following pathway A requires overcoming a prohibitive activation energy barrier of ~200 kJ mol^{-1} (172 kJ mol^{-1} for the periodic model and 208 kJ mol^{-1} for the cluster approach), while the initial displacement of a thioether group in pathway B clearly facilitates H–H rupture, with calculated activation energies of 5 and 42 kJ mol^{-1} for the periodic and cluster approaches, respectively. The similarity of geometries, elementary steps and energies confirms that the cluster model extracted from the periodic structure is adequate to perform the mechanistic study, and that saturating nitrogen atoms with hydrogen instead of Cu^{2+} does not alter significantly the results obtained.

The optimal experimental conditions for the semihydrogenation of acetylene correspond to a hydrogen-rich environment, with a H_2:acetylene ratio of 10:1. Therefore, the probability of finding two H_2 molecules close to the Pd_1Au_1 cluster as described in pathway C for H_2 dissociation is high. Under these reaction conditions, the possibility that the hydrogen atoms located at the Pd_1–Au_1 bridge sites could participate in the hydrogenation reaction needs to be further addressed. For that, new computational models were performed (Supplementary Fig. 34). The models showed that, after the dissociation of the first H_2 molecule, at least one of the two hydrogen atoms occupies a stable position at the Pd_1–Au_1 bridge sites (see structures 2-A and 2-B). Then, acetylene adsorbs bicoordinated to the palladium atom (structures 3-A and 3-B) and the first hydrogen-transfer step occurs, leading to formation of a C_2H_3 species monocoordinated to palladium, while the other hydrogen atom remains at the Pd_1–Au_1 bridge sites (structures 4-A and 4-B). At this point, all our efforts to find a transition state for the attack of the bridged hydrogen atom to the C_2H_3 species failed, using either the cluster approach or the periodic models. In contrast, coadsorption of a second H_2 molecule close to or on the palladium atom (structures 5-A and 5-B) and its subsequent dissociation forming directly adsorbed ethylene (structures 6-A and 6-B) is straightforward and energetically feasible. After ethylene desorption, unreacted structures 2-A or 2-B with the bridged hydrogen atom are regenerated, ready to interact with another acetylene molecule and start a new catalytic cycle.

Additionally, to also consider the effect of temperature on the energy barrier of the reaction, we constructed continuous energy and Gibbs free-energy profiles under standard state conditions (1 atm and 298 K) for hydrogen dissociation and acetylene semihydrogenation. For that, we follow pathways A and B (Supplementary Fig. 35). As expected, the Gibbs free energies (dashed lines) are higher than the electronic energies (full lines) and follow the same trends when comparing the two proposed pathways. Pathway A involves more stable minima and higher activation barriers, whereas pathway B is smoother, thus facilitating the catalytic cycle. The absolute activation energies and Gibbs free energies confirm the feasibility of pathway B (Supplementary Table 11).

The large difference in the calculated activation energies for H_2 dissociation following pathways A and B is due to the different way of interaction of H_2 with palladium, which leads to an easier rupture of the H–H bond in pathway B. The three-dimensional arrangement of the active site in the MOF makes it difficult to observe the geometry differences in the images in Fig. 4 or Supplementary Fig. 34, and therefore, to facilitate this analysis, the reactants (1-A and 1-B), transition states (TS12-A and TS12-B) and products (2-A and 2-B) are schematized in Supplementary Fig. 36, and the most important optimized distances are summarized in Supplementary Table 12. It should be noted that similar geometric parameters are obtained using cluster and periodic models. For the reactant 1-A, H_2 interacts with the palladium atom at the opposite side of the gold atom, so that one of the two hydrogen atoms migrates a long way to reach the bridge position between gold and palladium in product 2-A. In the transition state TS12-A, the migrating hydrogen atom is perpendicularly attached to a tetra-coordinated palladium atom, far from the other hydrogen atom (2.29 Å) and from gold (2.7–2.8 Å). The low stability of this transition state is explained by the fact that the migrating hydrogen atom is only stabilized by one bond with palladium. In contrast, in reactant 1-B, H_2 interacts with palladium in the neighbourhood of the Au–Pd bond, leading to an improved activation of the H–H bond (optimized bond distance (r_{H-H}) < 0.8 Å in 1-A and 0.8–0.9 Å in 1-B). In addition, H_2 dissociation through transition state TS12-B is facilitated by closer interactions between the migrating hydrogen atom and the other hydrogen atom (optimized r_{H-H} = 1.34 and 1.18 Å in the cluster and periodic models) and with gold (1.55 and 1.88 Å in the cluster and periodic models). Such additional interactions make TS12-B clearly more stable than TS12-A. Additional amplified views of 2-A, 3-A, 2-B and 3-B depicted in Supplementary Fig. 37 show that the relative orientation of the hydrogen atom on palladium, the two sulfur atoms and the adsorbed acetylene in 3-A come directly from 2-A, while adsorption of acetylene in 2-B produces the displacement of one bridged hydrogen to its position in 3-B.

Regarding the adsorption of acetylene and ethylene on the Pd–Au sites, because this is occurring in an olefin-rich environment, a preferential desorption or hydrogenation of ethylene has to be considered. To clarify this issue, we performed calculations using the periodic approach, including the whole structure of the MOF and all relevant interactions present in the environment of the active site. Taking into account the mechanism proposed, two different models of the active site were considered: a clean PdAu dimer present only at the beginning of the reaction; and structure 2-B with two adsorbed hydrogen atoms, that is, the initial and final state of the true catalytic cycle. Since the absolute value of the computed van der Waals interactions depends on the total number of atoms of the system, all calculated interaction energies are systematically larger for ethylene than for acetylene; thus, to make a reliable comparison, we took the initial state of acetylene or ethylene placed in the interstitial region of the MOF as a reference, close to the active site but not yet interacting with it (Supplementary Fig. 38). Attempts to adsorb acetylene or ethylene on the gold atom of the active site led to this same reference initial state, confirming that it is stable,

and suitable as a reference state. Adsorption of acetylene and ethylene on the palladium atom led to stable structures in which the molecule is always π-bonded to the palladium atom (Supplementary Fig. 38c,d). The calculated interaction energies relative to the reference state are larger on the clean Pd_1Au_1 dimer than on the 2-B site, and in both cases slightly larger for acetylene than for ethylene (Supplementary Table 13), confirming a preferential adsorption of acetylene on the active sites.

The transfer of electrons from palladium to gold is also justified by analysis of the Bader atomic charges on palladium and gold obtained from periodic DFT calculations of different catalyst models (Supplementary Table 10). The net atomic charges on palladium and gold in single-atom **Pd_1@1** and **Au_1@1** catalyst models, with the palladium and gold atoms placed in two different positions within the MOF (in the channels and in the interstitial regions), show a slightly positive charge, ~0.1*e* for palladium and ~0.2*e* for gold, whereas the computed charges for six different locations of the PdAu dimer (labelled A–F) give a net positive charge on palladium, increased between 0.05*e* and 0.5*e*, while the gold atoms become close to neutral or even slightly negatively charged in some cases. The only exception is the structure PdAu–C, in which the dimer is broken (r_{Au-Pd} = 2.24 Å) and the two metal atoms behave as individual species, both positively charged.

Conclusions

The semihydrogenation reaction of acetylene in ethylene streams under simulated industrial (front-end) conditions proceeds with ≥99.99% yield (≤1 ppm of acetylene remaining) and up to 94% selectivity with a well-defined catalyst composed of a molecular $Pd^{\delta+}$–Au^0 dimer prepared and supported, in situ, on a thioether-functionalized MOF. The performance of this material is remarkable in comparison to existing catalysts, since it works under a nearly barrierless activation energy (~1 kcal mol^{-1}), at temperatures ranging from 35 to 150 °C, with ethane as the only by-product. A combined experimental and computational mechanistic study reveals that the palladium atom acts as the main catalytic site while the gold atom and the thioether moieties of the MOF assist during the H_2 dissociation step. This study provides insights into the mechanism of this industrial reaction and join the concepts of single isolated catalytic sites and alloying on a heterometallic catalyst at the atomic level.

Methods

Materials

All chemicals were of reagent-grade quality. They were purchased from commercial sources and used as received. Crystals/polycrystalline samples of {Cu_6Sr[(*S*,*S*)-mecysmox]$_3$(OH)$_2$(H_2O)}·15H_2O (**1**) were prepared as previously reported[33] (Supplementary Methods).

$Pd_{0.5}Au_{0.5}$@{$Sr^{II}Cu^{II}_6$[(*S*,*S*)-mecysmox]$_3$(OH)$_2$(H_2O)}·12H_2O (Pd_1Au_1@1)

Well-formed green prisms of **Pd_1Au_1@1**, suitable for X-ray diffraction, were obtained by following a dual-step postsynthetic process. First, crystals of **1** (~5 mg) were suspended, alternately, in $AuCl_3$ and $[Pd(NH_3)_4]Cl_2$ H_2O/CH_3OH (1:2) solutions (0.2 mmol of the corresponding gold or palladium salt per mmol of **1**) for 90 min. The process was repeated five times and the resulting solid was then, in a second postsynthetic step, suspended in 5 ml of another H_2O/CH_3OH (1:2) solution to which an excess of $NaBH_4$, divided into 12 fractions (each fraction consisting of 1 mole of $NaBH_4$ per mole of **1**), was added progressively over 72 h. After each addition, the mixture was allowed to react for 1.5 h. After this period, samples were gently washed with an H_2O/CH_3OH solution and filtered on paper. Analysis: calculated (%) for $Cu_6SrAu_{0.5}Pd_{0.5}C_{30}H_{64}S_6N_6O_{33}$ (1,849.8): C, 19.48; H, 3.49; S, 10.40; N, 4.54. Found: C, 19.39; H, 3.33; S, 10.49; N, 4.55. Infrared (KBr): ν = 3,013, 2,961 and 2,914 cm^{-1} (C–H), 1,601 cm^{-1} (C=O).

A gramme-scale procedure, for catalytic experiments, was also carried out by using the same synthetic procedure but with greater amounts of a powder sample of **1** (5 g, 3 mmol) and equivalent amounts of $AuCl_3$, $[Pd(NH_3)_4]Cl_2$ and $NaBH_4$ with the same successful results and a very high yield (4.90 g, 93%). Analysis: calculated (%) for $Cu_6SrAu_{0.5}Pd_{0.5}C_{30}H_{64}S_6N_6O_{33}$ (1,849.8): C, 19.48; H, 3.49; S, 10.40; N, 4.54. Found: C, 19.29; H, 3.29; S, 10.40; N, 4.57. Infrared (KBr): ν = 3,011, 2,954 and 2,911 cm^{-1} (C–H), 1,606 cm^{-1} (C=O).

Further details of the material preparation can be found in the Supplementary Methods.

SCXRD

Crystal data for **Pd_1Au_1@1**: $C_{30}H_{64}Au_{0.50}Cu_6N_6O_{33}Pd_{0.50}S_6Sr$, hexagonal, space group $P6_3$, T = 296(2) K, Z = 2, a = 17.9333(11) Å, c = 12.8570(9) Å, V = 3,580.9(5) Å^3, ρ_{calc} = 1.716 g cm^{-3}, μ = 3.880 mm^{-1}. Further details can be found in the Supplementary Information.

Competitive adsorption of acetylene/ethylene

High-resolution isotherms were measured using a Micromeritics ASAP 2010 volumetric instrument. Approximately 50 mg of **Pd_1Au_1@1** in powder form was employed for these experiments. The sample was placed within a glass sample holder and immersed in a liquid circulation thermostatic bath to ensure precise temperature control. Prior to the adsorption experiments, the sample underwent overnight outgassing at 373 K under high vacuum. Isotherms were measured using pure ethylene on one hand, while a gas mixture comprising 1% acetylene in ethylene was utilized on the other hand. The adsorption isotherm was then obtained at 298 K while maintaining the sample at a constant temperature throughout the experiment. Further details can be found in the Supplementary Methods.

Microscopy measurements

High-angle annular dark-field scanning transmission electron microscopy measurements were performed on a double-aberration-corrected, monochromated, FEI Titan3 Themis 60-300 microscope working at 300 kV. Further details can be found in the Supplementary Methods.

XPS measurements

Samples were prepared by sticking, without sieving, the MOF onto a molybdenum plate with cellophane tape, followed by air drying. Measurements were performed on a K–Alpha XPS system using a monochromatic Al Kα source (1,486.6 eV). Further details can be found in the Supplementary Methods.

^{13}C ss-MAS-NMR with a ^{13}CO probe

^{13}C ss-MAS-NMR spectra were recorded on a Bruker AVIII HD 400 WB spectrometer using a 3.2 mm probe spinning the sample at 15 kHz, using 4 µs π/2 pulses for ^{13}C, with ^{1}H decoupling during acquisition and 5 s as recycle delay. Further details can be found in the Supplementary Methods.

X-ray adsorption spectroscopy techniques

XANES and EXAFS measurements were carried out on the NOTOS beamline at the ALBA Synchrotron Light Source, Barcelona, Spain. Further details can be found in the Supplementary Methods.

Catalytic experiments

Hydrogenation reactions. The gas-phase hydrogenation was studied for acetylene (1%) in ethylene (99%). The reactions were carried out in a packed bed reactor with 5–35 mg of MOF catalyst, at a total flow rate of 10–150 ml min^{-1}, without any inert carrier gas. Hydrogen was fed at stoichiometries of 80:1 to 1:30 with respect to the total moles of ethylene fed to the reactor, but usually performed at stoichiometries of 1:10–1:30. The reactions were followed by online gas chromatography, performed in a column suitable for the separation of C1–C6 hydrocarbons. The reactor was purged for 30 min with 20 ml min^{-1} N_2 after loading the catalyst, and then heated to the reaction temperature.

The reaction temperatures studied ranged from 30 °C to 150 °C. Before starting the reactions, the reagent was flowed through the reactor bypass and the areas were calibrated on the gas chromatograph. The catalyst was placed in the centre of the reactor tube, packed between glass wool. SiO_2 was used as a filler and refractory material for the tubular reactor; blank experiments show that any conversion occurs in its presence.

Cleaning of Pd_1Au_1@1 by Soxhlet extraction. After using the material to catalyse the acetylene semihydrogenation reaction, the packed bed was recovered from the reactor and sieved to remove the glass wool. The recovered catalyst (60–80%) was placed on filter paper and introduced into a Soxhlet set-up for extraction with dichloromethane, which was placed in a 250 ml flask on top of a stir plate programmed at a temperature of 70 °C. The extraction was left running for 1 h (approximately ten fill and wash cycles in the Soxhlet set-up). The contents of the extraction were analysed by gas chromatography–mass spectrometry.

H_2–D_2 isotope exchange. A fixed-bed reactor was loaded with 2 mg of **Pd_1Au_1@1**. After maintaining an argon flow rate of 18 ml min^{-1} for 20 min, 1 ml min^{-1} H_2 and 1 ml min^{-1} D_2 were added to the argon stream (total flow rate, 20 ml min^{-1}). This mixture of Ar, H_2 and D_2 was flowed for 15 min through the reactor bypass to calibrate the signal and then for approximately 15 min through the fixed bed to obtain the measurement. The pressure was kept constant at 1 bar, and the temperature was maintained at 30 °C throughout the experiment. The same experimental procedure was repeated with a 6 mg sample of **Pd_1Au_1@1**. The compounds at the reactor exit (H_2, D_2, HD) were quantified by online mass spectrometry (m/z = 2, 4 and 3, respectively).

Data availability

All data supporting the findings of this work are available from the corresponding authors on request. Crystallographic data for the structure reported in this paper have been deposited in the Cambridge Structural Database with CCDC number 2249968.

References

1. Martín, A. J., Mondelli, C., Jaydev, S. D. & Pérez-Ramírez, J. Catalytic processing of plastic waste on the rise. *Chem* **7**, 1487–1533 (2021).
2. Shittu, T. D. & Ayodele, O. B. Catalysis of semihydrogenation of acetylene to ethylene: current trends, challenges, and outlook. *Front. Chem. Sci. Eng.* **16**, 1031–1059 (2022).
3. Szesni, N. et al. Catalyst composition for selective hydrogenation with improved characteristics. US patent 13/276,403 (2013).
4. Zou, S. et al. Grafting nanometer metal/oxide interface towards enhanced low-temperature acetylene semihydrogenation. *Nat. Commun.* **12**, 5770 (2021).
5. Pei, G. X. et al. Performance of Cu-alloyed Pd single-atom catalyst for semihydrogenation of acetylene under simulated front-end conditions. *ACS Catal.* **7**, 1491–1500 (2017).
6. Pei, G. X. et al. Promotional effect of Pd single atoms on Au nanoparticles supported on silica for the selective hydrogenation of acetylene in excess ethylene. *New J. Chem.* **38**, 2043–2051 (2014).
7. Pei, G. X. et al. Ag alloyed Pd single-atom catalysts for efficient selective hydrogenation of acetylene to ethylene in excess ethylene. *ACS Catal.* **5**, 3717–3725 (2015).
8. Li, R. et al. Selective hydrogenation of acetylene over Pd–Sn catalyst: identification of Pd_2Sn intermetallic alloy and crystal plane-dependent performance. *Appl. Catal. B* **279**, 119348 (2020).
9. Pachulski, A., Schödel, R. & Claus, P. Performance and regeneration studies of Pd–Ag/Al_2O_3 catalysts for the selective hydrogenation of acetylene. *Appl. Catal. A* **400**, 14–24 (2011).
10. Hu, M. et al. MOF-confined sub-2 nm atomically ordered intermetallic PdZn nanoparticles as high-performance catalysts for selective hydrogenation of acetylene. *Adv. Mater.* **30**, 201801878 (2018).
11. Huang, F. et al. Atomically dispersed Pd on nanodiamond/graphene hybrid for selective hydrogenation of acetylene. *J. Am. Chem. Soc.* **140**, 13142–13146 (2018).
12. Qin, C., Guo, Q., Guo, J. & Chen, P. Atomically dispersed Pd atoms on a simple MgO support with an ultralow loading for selective hydrogenation of acetylene to ethylene. *Chem. Asian J.* **16**, 1225–1228 (2021).
13. Tejeda-Serrano, M. et al. Isolated Fe(III)–O sites catalyze the hydrogenation of acetylene in ethylene flows under front-end industrial conditions. *J. Am. Chem. Soc.* **140**, 8827–8832 (2018).
14. Wang, J. et al. Au@Pt nanotubes within CoZn-based metal-organic framework for highly efficient semihydrogenation of acetylene. *iScience* **23**, 101233 (2020).
15. Bu, J. et al. Selective electrocatalytic semihydrogenation of acetylene impurities for the production of polymer-grade ethylene. *Nat. Catal.* **4**, 557–564 (2021).
16. Guo, Y. et al. Photo-thermo semihydrogenation of acetylene on Pd/TiO single-atom catalyst. *Nat. Commun.* **13**, 2648 (2022).
17. Yang, Z. et al. Al_2O_3 microrods-supported Pd catalysts for semihydrogenation of acetylene: acidic properties tuned reaction kinetics behaviors. *Chem. Eng. J.* **445**, 136681 (2022).
18. Zhang, W. et al. Bismuth-modulated surface structural evolution of Pd_3Bi intermetallic alloy catalysts for selective propane dehydrogenation and acetylene semihydrogenation. *ACS Catal.* **12**, 10531–10545 (2022).
19. Xu, L. et al. Anchoring Pd species over defective alumina to achieve high atomic utilization and tunable electronic structure for semihydrogenation of acetylene. *Appl. Catal. A* **642**, 118690 (2022).
20. Ru, W. Control of local electronic structure of Pd single atom catalyst by adsorbate induction. *Small* **18**, 2103852 (2022).
21. Luo, Q. et al. Alloyed PdCu nanoparticles within siliceous zeolite crystals for catalytic semihydrogenation. *ACS Mater. Au* **2**, 313–320 (2022).
22. Delgado, J. A. et al. Controlled one-pot synthesis of PdAg nanoparticles and their application in the semihydrogenation of acetylene in ethylene-rich mixtures. *ChemNanoMat* **8**, e202200058 (2022).
23. Liu, Y. et al. Polyoxometalate-based metal-organic framework as molecular sieve for highly selective semihydrogenation of acetylene on isolated single Pd atom sites. *Angew. Chem. Int. Ed.* **60**, 22522–22528 (2021).
24. Song, Y. et al. Understanding the role of coordinatively unsaturated Al sites on nanoshaped Al for creating uniform Ni–Cu alloys for selective hydrogenation of acetylene. *ACS Catal.* **13**, 1952–1963 (2023).
25. Wang, J., Xu, H., Che, C., Zhu, J. & Cheng, D. Rational design of PdAg catalysts for acetylene selective hydrogenation via structural descriptor-based screening strategy. *ACS Catal.* **13**, 433–444 (2023).
26. Kley, K. S., De Bellis, J. & Schueth, F. Selective hydrogenation of highly concentrated acetylene streams over mechanochemically synthesized PdAg supported catalysts. *Catal. Sci. Technol* **13**, 119–131 (2023).
27. Huang, F. et al. Low-temperature acetylene semihydrogenation over the Pd-Cu dual-atom catalyst. *J. Am. Chem. Soc.* **144**, 18485–18493 (2022).
28. Jian, M., Liu, J.-X. & Li, W.-X. Hydroxyl improving the activity, selectivity and stability of supported Ni single atoms for selective semihydrogenation. *Chem. Sci* **12**, 10290–10298 (2021).

29. Feng, H. et al. Machine-learning-assisted catalytic performance predictions of single-atom alloys for acetylene semihydrogenation. *ACS Appl. Mater. Interfaces* **14**, 25288–25296 (2022).
30. Furukawa, H., Cordova, K. E., O'Keeffe, M. & Yaghi, O. M. The chemistry and applications of metal–organic frameworks. *Science* **341**, 974 (2013).
31. Kitagawa, S. & Matsuda, R. Chemistry of coordination space of porous coordination polymers. *Coord. Chem. Rev.* **251**, 2490–2509 (2007).
32. Escamilla, P. et al. Metal–organic frameworks as chemical nanoreactors for the preparation of catalytically active metal compounds. *Chem. Commun.* **59**, 836–851 (2023).
33. Tiburcio, E. et al. Soluble/MOF-supported palladium single atoms catalyze the ligand-, additive-, and solvent-free aerobic oxidation of benzyl alcohols to benzoic acids. *J. Am. Chem. Soc.* **143**, 2581–2592 (2021).
34. Rivero-Crespo, M. A. et al. Confined Pt_1^{1+} water clusters in a MOF catalyze the low-temperature water–gas shift reaction with both CO_2 oxygen atoms coming from water. *Angew. Chem. Int. Ed.* **57**, 17094–17099 (2018).
35. Mon, M. et al. Synthesis of densely packaged, ultrasmall PtO_2 clusters within a thioether-functionalized MOF: catalytic activity in industrial reactions at low temperature. *Angew. Chem. Int. Ed.* **57**, 6186–6191 (2018).
36. Tiburcio, E. et al. Highly efficient MOF-driven silver subnanometer clusters for the catalytic Büchner ring expansion reaction. *Inorg. Chem.* **61**, 11796–11802 (2022).
37. Fortea-Pérez, F. R. et al. The MOF-driven synthesis of supported palladium clusters with catalytic activity for carbene-mediated chemistry. *Nat. Mater.* **16**, 760–766 (2017).
38. Reina, M., Wallace, W. T., Wyrwas, R. B., Whetten, R. L. & Martínez, A. Binding of multiple SO_2 molecules to small gold cluster anions (Au_N^-, Au_NOH^-, N=1–8). *Int. J. Quantum Chem.* **119**, e25987 (2019).
39. Dobrzyńska, J., Dąbrowska, M., Olchowski, R. & Dobrowolski, R. An ion-imprinted thiocyanato-functionalized mesoporous silica for preconcentration of gold(III) prior to its quantitation by slurry sampling graphite furnace AAS. *Microchim. Acta* **185**, 564 (2018).
40. Oliver-Meseguer, J. et al. Generation and reactivity of electron-rich carbenes on the surface of catalytic gold nanoparticles. *J. Am. Chem. Soc.* **140**, 3215–3218 (2018).
41. Silva, T. A. G. et al. Restructuring of gold-palladium alloyed nanoparticles: a step towards more active catalysts for oxidation of alcohols. *ChemCatChem* **11**, 4021–4027 (2019).
42. Nishimura, S., Ikeda, N. & Ebitani, K. Selective hydrogenation of biomass-derived 5-hydroxymethylfurfural (HMF) to 2,5-dimethylfuran (DMF) under atmospheric hydrogen pressure over carbon supported PdAu bimetallic catalyst. *Catal. Today* **232**, 89–98 (2014).
43. Cerezo-Navarrete, C. et al. Ruthenium nanoparticles canopied by heptagon-containing saddle-shaped nanographenes as efficient aromatic hydrogenation catalysts. *Chem. Sci.* **13**, 13046–13059 (2022).
44. Hyun, K. et al. Tailoring a dynamic metal–polymer interaction to improve catalyst selectivity and longevity in hydrogenation. *Angew. Chem. Int. Ed.* **60**, 12482–12489 (2021).
45. Dong, J., Robinson, J. R., Gao, Z.-H. & Wang, L.-S. Selective semihydrogenation of polarized alkynes by a gold hydride nanocluster. *J. Am. Chem. Soc.* **144**, 12501–12509 (2022).
46. Campos, J. Dihydrogen and acetylene activation by a gold(I)/platinum(0) transition metal-only frustrated Lewis pair. *J. Am. Chem. Soc.* **139**, 2944–2947 (2017).
47. Dasgupta, A. et al. Atomic control of active-site ensembles in ordered alloys to enhance hydrogenation selectivity. *Nat. Chem.* **14**, 523–529 (2022).
48. Gao, R. et al. Pd/Fe_2O_3 with electronic coupling single-site Pd–Fe pair sites for low-temperature semihydrogenation of alkynes. *J. Am. Chem. Soc.* **144**, 573–581 (2022).

Acknowledgements

Financial support by the projects PID2020-115100GB-I00, PID2020-112590GB-C21, PID2019-104778GB-I00, CEX2021-001230-S and CEX2019-000919-M (funded by the Spanish MCIINN) is acknowledged. We also acknowledge the Generalitat Valenciana (SEJI/2020/034 and PROMETEO/2021/054), the Ministero dell'Istruzione, dell'Università e della Ricerca (project code PE0000021, 'Network 4 Energy Sustainable Transition – NEST') and the European Research Council (814804, MOF-reactors). J.F.-S. thanks the Ramón y Cajal programme (RYC2019-027940-I). N.M. and M.M. thank the Juan de la Cierva programme for a contract (MCIINN, FJC2018-035455-I and FJC2019-040523-I, respectively). M.B. thanks the Instituto de Tecnología Química for the concession of a contract. High-resolution scanning transmission electron microscopy was performed at DME-UCA, Cadiz University with financial support from FEDER/MINECO (PID2019-110018GA-I00 and PID2019-107578GA-I00). We also thank Diamond Light Source for the award of beamtime (I19 beamline) and provision of synchrotron radiation facilities (proposal CY28808-1). Thanks are also extended for a scholarship (ID 100010434) LCF/BQ/DI19/11730029 (J.B.-S) from 'La Caixa' Foundation. Computations were performed on the Tirant III cluster of the Servei d'Informàtica of the University of Valencia. This study forms part of the Advanced Materials programme (MFA/2022/048) and was supported by MCIINN with funding from European Union NextGenerationEU (PRTR–C17.I1) and by Generalitat Valenciana. We are grateful to A. Vidal and M. Palomino for performing the NMR and acetylene adsorption experiments, respectively.

Author contributions

J.B.-S. performed and interpreted the flow reactions and the experimental mechanistic experiments. N.M. and E.T. carried out the synthesis of the MOF materials. M.B. carried out the flow reactions and prepared the zeolites. M.M. performed some of the material characterizations. J.C.H.-G. carried out and interpreted the microscopy measurements. C.M. carried out the X-ray adsorption spectroscopy experiments. M.B. carried out and supervised the computational studies. J.F.-S. designed the MOF synthesis and interpreted the results. D.A. performed, resolved and interpreted the SCXRD experiments. E.P. supervised the synthesis and characterization of the material and wrote the paper, and A.L.-P. supervised the catalytic part and wrote the paper. All authors contributed to writing the paper.

Competing interests

A patent application has been filed and presented in Spain, with application number P202330601; J.B.-S., M.B., J.F.-S., E.P. and A.L.-P. appear as inventors. The other authors declare no competing interests.

Additional information

Supplementary information The online version contains supplementary material available at https://doi.org/10.1038/s41929-024-01130-7.

Correspondence and requests for materials should be addressed to Donatella Armentano, Emilio Pardo or Antonio Leyva-Pérez.

Peer review information *Nature Catalysis* thanks Dingsheng Wang, Xin Zhang and the other, anonymous, reviewer(s) for their contribution to the peer review of this work.